Effects of local stress, strain, and hydrogen content on hydrogen-related fracture behavior in low-carbon martensitic steel

Akinobu Shibata, Takashi Yonemura, Yuji Momotani, Myeong-Heom Park, Shusaku Takagi, Yazid Madi, Jacques Besson, Nobuhiro Tsuji

Effects of local stress, strain, and hydrogen content on hydrogen-related fracture behavior in low-carbon martensitic steel

Akinobu Shibata [1-4,*], Takashi Yonemura [2], Yuji Momotani [2], Myeong-heom Park [3], Shusaku Takagi [5], Yazid Madi [4], Jacques Besson [4], Nobuhiro Tsuji [2,3]

[1] Research Center for Structural Materials, National Institute for Materials Science (NIMS), 1-2-1, Sengen, Tsukuba 305-0047, Japan.

[2] Department of Materials Science and Engineering, Kyoto University, Yoshida-honmachi, Sakyo-ku, Kyoto 606-8501, Japan.

[3] Elements Strategy Initiative for Structural Materials (ESISM), Kyoto University, Yoshida-honmachi, Sakyo-ku, Kyoto 606-8501, Japan.

[4] Centre des Matériaux, MINES ParisTech, CNRS UMR 7633, BP 87, 91003, Evry, France

[5] Steel Research Laboratory, JFE Steel Corporation, 1-1, Minamiwatarida-cho, Kawasaki-ku, Kawasaki 210-0855, Japan

[*] Corresponding author E-mail: SHIBATA.Akinobu@nims.go.jp

Tel: +81-29-859-2074

Abstract

The present study investigated the hydrogen-related fracture behavior of specimens with different stress concentration factors through microstructure observation, finite element (FE) simulation, and digital image correlation (DIC) analysis. The alloy studied was a simple model alloy (Fe-0.2C binary alloy) with fully martensite structure. When the hydrogen content was large (2.21 mass ppm (121 at ppm)), the crack initiation and propagation occurred along the prior austenite grain boundaries. Through the FE simulations, we found that the crack initiation sites corresponded to the region with high stress and high hydrogen content. Although the stress concentration factors were different, the stress level and the hydrogen content at the crack initiation sites were almost the same, indicating that the hydrogen-related intergranular fracture originated from stress-controlled decohesion at the prior austenite grain boundaries. For the specimen with small hydrogen content (0.41 mass ppm (22.5 at ppm)), the quasi-cleavage cracks formed at the surface of the notch root and propagated along the {011} planes. The FE simulations revealed that the plastic strains were maximum at the initiation sites of the quasi-cleavage cracks. Moreover, we confirmed that hydrogen enhanced the local plastic deformation by DIC analysis. As the local values of maximum principal stress, plastic strain ~~amount~~, and hydrogen content at the initiation sites of the quasi-cleavage cracks were different depending on the stress concentration factor, the critical quantitative condition for the initiation of quasi-cleavage cracking was not simple compared to that of the case of intergranular cracking.

Keywords; hydrogen embrittlement; martensite; stress and strain; finite-element simulation; digital

image correlation

1. Introduction

Recently, the demand for high-strength steel has been increasing from economic and environmental viewpoints. As the susceptibility of high-strength steel, particularly martensitic steel, to hydrogen embrittlement is considerably high, one of the issues in the practical application of high-strength steel is hydrogen embrittlement. Several models have been proposed to account for the hydrogen-related fracture [1, 2]. However, to date, the underlying mechanism for hydrogen-related fracture is yet to be fully understood.

Low and medium carbon martensitic steels comprise several structural units with different length scale: lath, block, packet, and prior austenite grain [3]. A lath is a single-crystal martensite plate with a thickness of about 0.2 μm, and boundaries between laths are low-angle boundaries with misorientation angle less than three degrees [3]. A block consists of many laths having nearly identical crystallographic orientation, and a packet consists of several blocks with nearly the same habit planes. As the name suggests, a prior austenite grain is a region corresponding to a single grain at austenite state. Typical modes of hydrogen-related fracture of martensitic steels are intergranular and quasi-cleavage. Intergranular fracture occurs due to a decrease in the cohesive energy at the boundary by the segregation of hydrogen [4-6]. In the case of martensitic steels, hydrogen-related intergranular fracture often occurs on prior austenite grain boundaries [7-13]. On the other hand, quasi-cleavage corresponds to a transgranular fracture occurring on non-typical cleavage planes [14, 15]. It is well known that increasing the hydrogen content changes the

fracture mode from quasi-cleavage to intergranular even in a given material [16]. Elucidating the critical factors that determine whether quasi-cleavage fracture or intergranular fracture occurs is one of the most important technical challenges in the research field of hydrogen embrittlement. Takeda and McMahon [17] conducted a pioneering study on the effect of strain and stress on hydrogen-related fracture modes. They studied the hydrogen-related fracture behavior of tempered martensitic steels with different impurity contents. The quasi-cleavage cracking occurred when the impurity segregation was small, while the specimen with a large amount of impurity segregation exhibited intergranular cracking. They proposed that the quasi-cleavage fracture corresponded to strain-controlled Mode II fracture and occurred along the planes of maximum shear stress. On the other hand, the intergranular cracking was stress-controlled decohesion at the prior austenite grain boundaries. However, their study also involved the effect of segregated impurities. Wang et al. [9] studied the effect of stress concentration on the hydrogen-related fracture behavior of tempered martensitic steel using notched round bar specimens with different notch root radii. The dominant mode of hydrogen-related fracture was intergranular. Their conclusion was that the local stress field (maximum principal stress) and the local hydrogen content controlled the intergranular cracking. Novak et al. [18] studied the initiation site of hydrogen-related intergranular cracking in tempered martensitic steel and revealed that the local event of intergranular cracking was stress-controlled as the fracture was initiated ahead of the notch root, typically near the elastic – plastic interface, where the local tensile stress was the highest. We

previously reported that the quasi-cleavage fracture occurred along the {011} crystallographic planes in both martensitic and ferritic steels [10, 12, 19-21]. Particularly, the references of [12, 21] definitively determined the crystallographic orientations of the quasi-cleavage facets by two-surface trace analysis and demonstrated that the quasi-cleavage fractures occurred along {011} planes. Several papers [22-25] proposed that the hydrogen-related quasi-cleavage fracture occurred on lath boundaries and / or block boundaries, because the crystallographic orientation of these boundaries are nearly parallel to {011} planes. However, we previously showed the clear evidence that the quasi-cleavage crack propagated inside the lath, not on the lath boundaries [12]. Moreover, we confirmed that the hydrogen-related quasi-cleavage fracture occurred along {011} planes even in a low carbon steel with a simple ferritic microstructure and proposed that the fracture on {011} planes was an intrinsic characteristic of hydrogen-related quasi-cleavage fracture in steels having body centered cubic (bcc) phases, not related with the complicated martensite microstructure [21]. Considering that {011} plane corresponds to slip planes in a bcc structure, plastic deformation would have an important role in quasi-cleavage fracture.

To deepen the understanding of the factors that determine the mode of hydrogen-related fracture, whether intergranular or quasi-cleavage, the present study investigated the hydrogen-related fracture behaviors under stress concentration conditions in as-quenched low-carbon martensite steel with different hydrogen content, and discussed the effects of local stress, strain, and hydrogen content on the mode of hydrogen-related fracture by utilizing an FE simulation.

2. Experimental Procedure

The steel used in the present study was an Fe-0.2C (mass %) binary alloy. The detailed chemical composition was C: 0.23, Si: < 0.02, Mn: < 0.02, P: < 0.005, S: < 0.0005, O: 0.0010, N: 0.0012, and Fe: bal. (mass %). The as-received steel with a thickness of 12 mm was cold-rolled to 1.7 mm thickness. The cold-rolled sheets were austenitized at 900 °C for 30 min in vacuum, followed by ice-brine quenching and sub-zero cooling in liquid nitrogen. The as-quenched specimens exhibited a fully martensitic structure. The heat-treated specimens were mechanically polished on both sides until a final thickness of 1 mm was reached to remove the decarburized layers formed during the heat treatment. Sheet-type smooth and double-notched tensile test specimens with a gauge length of 10 mm, gauge width of 5 mm, and gauge thickness of 1 mm were prepared by spark wire cutting. As shown in the schematic illustration of **Figure 1(a)**, the notch radii are 1 mm and 0.25 mm, and the un-notched ligament length is 2.5 mm. The stress concentration factors (Kt) of the specimens with notch radii of 1 mm and 0.25 mm are 2.1 and 3.2, respectively.

The double-notched tensile test specimens were cathodically pre-charged with hydrogen in an aqueous solution of 3 % NaCl and 3 g L^{-1} NH_4SCN for 24 h at room temperature. The current density of the hydrogen charging was 0.625 A m^{-2} or 1 A m^{-2}. A platinum plate was used as the counter electrode. The diffusible hydrogen contents (H_D) of the specimens at the current densities

of 0.625 A m^{-2} and 1 A m^{-2}, measured by thermal desorption analysis (TDA), were 0.41 mass ppm (22.5 at ppm) and 2.21 mass ppm (121 at ppm), respectively. The desorption profiles are presented in **Figure 2** (open circles: 0.625 A m^{-2}, solid circles: 1 A m^{-2}). The calibration of the TDA was performed by using a mixture gas of Ar + H_2. Here, H_D was defined as the cumulative hydrogen content desorbed below 300 °C, where the first TDA peak ended. Slow strain rate tensile tests at a crosshead speed of 5×10^{-3} mm min^{-1} were performed at room temperature in air. An extensometer was used to measure the displacement of the gauge area. The TDA measurements and the slow strain rate tensile tests were always started 40 min after the completion of the hydrogen charging.

The fracture surfaces of the tensile-tested specimens were observed using scanning electron microscopy (SEM, JEOL: JSM-7800F). To investigate the crack initiation and propagation behaviors, some of the slow strain rate tensile tests were stopped just after reaching the maximum stress. Then, a Ni layer was electroplated onto the tensile-tested specimen to preserve the cracks near the notch root. An aqueous solution of 150 g L^{-1} Ni_2SO_4 + 15 g L^{-1} H_3BO_4 was used as the electrodeposition solution. Plating was performed at room temperature and at a current density of 100 A m^{-2} with a plating time of 24 h. Crystal orientation mappings on the mid-thickness sections of the tensile-tested specimens were performed by electron backscattering diffraction (EBSD) using SEM (JEOL JSM-7100F) operated at 15 kV. The specimen surfaces for the EBSD measurements were prepared by electrolytic polishing in a solution of 90 % CH_3COOH and 10 % $HClO_4$. The

EBSD measurement and analysis were performed with the TSL OIM Data Collection program and the TSL OIM Analysis program, respectively.

Elasto-plastic FE simulations were carried out using the commercial Z-set software [26, 27] to compute the local stress, strain, and hydrogen distributions around the notch root region. The FE meshes used for simulation are shown in **Figure 1(b)**. Owing to the symmetry, one-eighth of the specimen geometry was meshed with reduced-integration quadratic elements (20 nodes 3D elements with 8 integration points). In order to obtain the material parameters for the FE simulation, the true stress – true strain curve of the uncharged smooth specimen (displacement rate: 5×10^{-3} mm min^{-1}) was fitted according to the following equation:

$$\sigma = \sigma_0 + Q_1(1 - \exp(-b_1\varepsilon)) + Q_2(1 - \exp(-b_2\varepsilon)) \qquad \text{Eq. 1}$$

where σ is the true stress, ε is the true plastic strain, σ_0, Q_1, Q_2, b_1, and b_2 are the fitting parameters. The fitted values of the parameters were σ_0 = 535.63 MPa, Q_1 = 296.88 MPa, Q_2 = 774.41 MPa, b_1 = 47.09, and b_2 = 222.18. A Young's modulus of 185.6 GPa (estimated from the stress – strain curve) and Poisson's ratio of 0.3 were used for the FE simulation.

To investigate the local plastic deformation behavior, the DIC technique was used. After hydrogen-charging and electrolytic polishing with the same solution used for the EBSD analysis specimens, SEM images of the specimen surface around the notch root region were taken. Subsequently, the specimen was tensile-deformed to the maximum stress and SEM images were taken again. The SEM images before and after the tensile deformation were analyzed using the

Correlated Solutions VIC-2D software.

3. Results

3.1 Mechanical properties

Figure 3 presents the engineering stress – displacement curves of the specimen with (a) Kt = 2.1 and (b) Kt = 3.2. Here, the engineering stress (s) is F / A_0, where F is the applied tensile load and A_0 is the initial cross-sectional area at the notch root. The tensile strengths of the uncharged specimens with Kt = 2.1 and Kt = 3.2 were 1741 MPa and 1780 MPa, respectively, and they did not significantly change with Kt. However, the elongation of the uncharged specimen with Kt = 3.2 was limited compared to that with Kt = 2.1. The hydrogen-charged specimens (Kt = 2.1 and Kt = 3.2) with H_D of 0.41 mass ppm (22.5 at ppm) exhibited some plasticity before the fracture, while those with H_D of 2.21 mass ppm (121 at ppm) fractured within the apparent elastic strain regimes. When the H_D was 0.41 mass ppm (22.5 at ppm), the fracture stress did not change significantly with Kt (1483MPa for Kt = 2.1 and 1430 MPa for Kt = 3.2). On the other hand, the fracture stress of the specimens with H_D of 2.21 mass ppm (121 at ppm) decreased from 980 MPa to 527 MPa when Kt increased from 2.1 to 3.2.

3.2 Fracture surface

The fracture surfaces of the uncharged specimens with Kt = 2.1 and Kt = 3.2 exhibited fully ductile surfaces with dimple patterns (images not shown). The SEM images showing the fracture surfaces of the hydrogen-charged specimens with Kt = 2.1 and H_D = 2.21 mass ppm (121 at ppm)

are presented in **Figure 4**. **Figure 4** shows **(a)** a low-magnification SEM image and **(b-d)** high magnification SEM images. Three types of surface morphologies are observed: ductile dimple surface (**Figure 4(b)**), quasi-cleavage surface (**Figure 4(c)**), and macroscopically intergranular surface **(Figure 4(d)**). The macroscopically intergranular surface was composed of a relatively smooth intergranular surface (indicated by white arrows) and intergranular-like surface with serrated markings (indicated by black arrows). We previously reported that the intergranular-like surface with serrated markings originated from the quasi-cleavage fracture propagated in the vicinity of the prior austenite grain boundaries [10-12]. Here, we confirmed that the fracture surfaces of all the hydrogen-charged specimens were quite similar to those in **Figure 4** and comprised ductile dimple surface, quasi-cleavage surface, and intergranular surface.

3.3 Crack initiation / propagation behaviors for large H_D (2.21 mass ppm (121 at ppm))

Figure 5 shows **(a, c)** SEM images and **(b, d)** EBSD orientation maps around the notch roots: **(a, b)** the specimen with Kt = 2.1, **(c, d)** the specimen with Kt = 3.2 when the H_D was large (2.21 mass ppm (121 at ppm)). The colors in the EBSD orientation map express the orientations parallel to the normal direction of the observed section according to the stereographic triangle below the EBSD orientation map. We found that several small and sharp cracks formed and propagated discontinuously at least on the observed section, indicating that the crack propagation was not uniform. For the specimen with Kt = 2.1 (**Figure 5(a)**), all the cracks exist ahead of the notch root surface. Simply assuming that the crack closest to the notch root surface was the initial crack

(though based on two-dimensional analysis), we considered that the crack was initiated about 50 μm away from the notch root surface. On the other hand, the crack connected to the notch root surface for the specimen with Kt = 3.2 (**Figure 5(c)**), implying that the crack was initiated at the notch root surface. In the EBSD orientation maps of **Figures 5(b, d)**, the positions of the block boundaries, packet boundaries, and prior austenite grain boundaries determined by the orientation analysis are indicated by the black solid lines, the yellow solid lines, and the white broken lines, respectively. We characterized the observed cracks in the EBSD orientation maps of **Figures 5(b, d)** as intergranular type or quasi-cleavage type. The intergranular crack components existing on the prior austenite grain boundaries are indicated by the red solid lines. In addition, the crack components parallel to the {011} plane traces are indicated by the orange solid lines. Our previous studies reported that hydrogen-related quasi-cleavage fracture occurred on {011} planes [10-12, 19-21]. Although the analysis on **Figure 5** was single-surface trace analysis and did not determine the exact orientation of crack plane, we can simply assume that the crack components parallel to {011} plane traces correspond to quasi-cleavage fracture based on our previous studies [10-12, 19-21]. We found that the initial cracks were intergranular-type for both the specimens with Kt = 2.1 and Kt = 3.2. Some of the quasi-cleavage cracks were observed at the regions far away from the notch root surfaces.

FE simulations were performed in order to estimate the local stress, strain, and hydrogen distributions around the notch root regions of the mid-thickness sections. Because clear crack

initiations could not be observed before reaching the maximum stress, the applied stress in the FE simulations was the same as the experimentally measured maximum stress (fracture stress). The equations to estimate local hydrogen content have been well documented in previous papers [28, 29], and are briefly summarized as follows. It can be considered that hydrogen at the normal interstitial sites and the reversible trapping sites, such as lattice defects, are always in equilibrium according to the following equation [30]:

$$\frac{\theta_T}{1-\theta_T} = \frac{\theta_L}{1-\theta_L} \exp\left(\frac{W_B}{RT}\right) \qquad \text{Eq.2}$$

where θ_L is the occupancy of the interstitial sites, θ_T is the occupancy of the trapping sites, W_B is the trap binding energy, R is the gas constant (8.31 J mol^{-1}), and T is the absolute temperature. The hydrogen atoms at the interstitial sites per unit volume, C_L, is expressed as $C_L = \theta_L \beta N_L$, where β is the number of interstitial sites per solvent atom, and N_L is the number of solvent atoms per unit volume. N_L is given by N_A / V_M, where N_A is Avogadro's number (6.0232×10^{23} mol^{-1}), and V_M is the molar volume of the host lattice. Similarly, the hydrogen atoms existing at the trapping sites per unit volume, C_T, is expressed as $C_T = \theta_T \alpha N_T(\varepsilon_p)$, where α is the number of hydrogen atom sites per trap, and $N_T(\varepsilon_p)$ is the trap density per unit volume expressed as a function of plastic strain (ε_p). Under a stress field, hydrogen tends to accumulate in the region where hydrostatic stress (σ_{kk}) is large and satisfies the following equilibrium:

$$\frac{\theta_L}{1-\theta_L} = \frac{{\theta_L}^0}{1-{\theta_L}^0} \exp\left(\frac{\sigma_{kk} V_H}{3RT}\right) \qquad \text{Eq.3}$$

where θ_L^0 is the initial occupancy of the interstitial sites without a stress field, and V_H is the partial

molar volume of hydrogen. Combining Eqs. 2 and 3, the total atomic concentration of hydrogen, c, can be expressed as:

$$c = \frac{C_L + C_T}{N_L} = \beta\theta_L + \alpha\frac{N_T(\varepsilon_p)}{N_L}\theta_T \qquad \text{Eq.4}$$

Seeger [31] reported that hydrogen was likely to exist at tetrahedral interstitial sites in iron, so that β is equal to 6. Hydrogen might be trapped at lath / block / packet boundaries in martensite structure. To date, however, there has been no clear evidence that hydrogen is likely to be trapped at these boundaries. Moreover, our previous experiments using hydrogen micro-print technique suggested that hydrogen was not trapped at any boundaries in martensite structure just after hydrogen charging [19], and that dislocation movement transported hydrogen to prior austenite grain boundaries during deformation [32]. Considering the fact that hydrogen trapping at boundaries in martensite structure has yet to be clarified, we simply assumed that most of the hydrogen was trapped by dislocations (W_B = 26.8 kJ mol^{-1} [33] in Eq.2 and α=1 in Eq.4). According to Taha and Sofronis [34], N_T is given by:

$$N_T = \frac{\sqrt{2}\rho}{a} \qquad \text{Eq.5}$$

where ρ is the dislocation density, and a is the lattice constant (0.28664 nm of pure iron was used in the present study). From the dislocation density data of the low-carbon martensitic steel measured by neutron diffraction [35], the relationship between ρ and ε_p was estimated to be ρ = 3.99872 × 10^{15} (1 + 5.159 ε_p) m^{-2}. We also assumed that hydrogen diffusion was fast enough so that the local hydrogen content reached the equilibrium value derived from Eq. 4 when the fracture occurred.

However, the total hydrogen content in the specimen obtained using Eq.4 becomes larger than that before applying deformation. According to Wang et al. [9], to keep the mass conservation law at the notched area, the hydrogen content obtained by Eq.4 was multiplied by a factor given by:

$$f = \frac{H_D \sum_i V_i}{\sum_i (V_i H_i)} \qquad \text{Eq.6}$$

where *Vi* is the volume of an element, and *Hi* is the hydrogen content of an element obtained from Eq.4. For the above calculations, the desorption of hydrogen during the tensile test was not taken into account. As shown in **Figure 2**, the desorption rate of the specimen at a current density of 0.625 A m^{-2} is almost zero around room temperature, implying that the hydrogen desorption during the tensile test at room temperature was small. When the current density was 1 A m^{-2}, on the other hand, the desorption rate at room temperature (22.8 °C) is 0.005975 mass ppm min^{-1}. Simple estimation for hydrogen desorption during the tensile test by using the value suggests that the amount of desorbed hydrogen until reaching the maximum stress is 0.310 mass ppm for the specimen with *Kt* = 2.1 and 0.191 mass ppm for the specimen with *Kt* = 3.2. These values are less than approximately 15 % of the total hydrogen content (2.21 mass ppm). Moreover, our previous paper [20] showed that about 10 % of total hydrogen was desorbed from the specimen during the tensile test (alloy composition, strain rate, and fractured strain were almost the same as those in the present study). Based on these facts, the present paper simply estimated local hydrogen concentrations using the Eqs. 1 ~ 6 without considering hydrogen desorption during the tensile tests.

Figure 6 shows the FE simulation results on the mid-thickness sections when H_D is 2.21 mass ppm (121 at ppm) for the specimens with **(a-f)** Kt = 2.1 and **(g-l)** Kt = 3.2: **(a-c, g-i)** distribution maps and **(d-f, j-l)** profiles at the notch root of **(a, d, g, j)** maximum principal stress (σ_p), **(b, e, h, k)** equivalent plastic strain (e_q), and **(c, f, i, l)** local hydrogen content (H_L). In addition, the positions of the initial cracks are indicated in each profile. It can be seen that the local hydrogen contents at the notch root regions are higher than the global hydrogen contents (**Figures 6 (f, l)**). For the specimen with Kt = 2.1 (**Figures 6 (a-f)**), the peak positions of the maximum principal stress and equivalent plastic strain are the notch root surface. On the other hand, the local hydrogen content is the highest at the position about 50 μm away from the notch root surface. In the case of the specimen with Kt = 3.2 (**Figures 6 (g-l)**), the peak positions of all the maximum principal stress, equivalent plastic strain, and local hydrogen content correspond to the surface of the notch root. In both the specimens, the plastic strain values are considerably small. We find that the maximum principal stress and the local hydrogen content at the positions of initial intergranular cracks in the specimen with Kt = 2.1 are σ_P = 1257 ~ 1283 MPa and H_L = 143 ~ 144 at ppm, respectively (**Figures 6 (d, f)**). As shown in **Figures 5 (c, d)**, the intergranular crack was initiated at the notch root surface in the specimen with Kt = 3.2. Though there still remains a possibility that the crack was initiated ahead of the notch and then grew back to the notch surface as deformation proceeded, the highest values of maximum principal stress, plastic strain, and local hydrogen content at the notch-root surface strongly support the crack initiation at the notch root surface. The maximum

principal stress and the local hydrogen content at the notch root surface are σ_P = 1212 MPa and H_L = 159 at ppm, respectively (**Figures 6 (j, l)**). This suggests that the intergranular cracks were initiated under almost the same local stress field and hydrogen content, even though the stress concentration factors were different.

3.4 Crack initiation / propagation behaviors for small H_D (0.41 mass ppm (22.5 at ppm))

Figure 7 shows the crack initiation and propagation behaviors when the H_D was small (0.41 mass ppm (22.5 at ppm)): **(a, b)** the specimen with Kt = 2.1, **(c, d)** the specimen with Kt = 3.2. The intergranular crack components and the quasi-cleavage crack components (parallel to the {011} plane traces) are indicated by the red solid lines and the orange solid lines, respectively, in **Figures 7 (b, d)**. In contrast with the case of larger H_D (**Figure 5**), the crack morphology (almost the largest opening displacement at the notch root surface) strongly suggests that one large crack formed at the notch root surface and propagated in a quasi-cleavage manner (parallel to the {011} plane traces) in both the specimens with Kt = 2.1 and Kt = 3.2.

Figure 8 shows the FE simulation results on the mid-thickness sections when H_D is 0.41 mass ppm (22.5 at ppm) for the specimens with **(a-f)** Kt = 2.1 and **(g-l)** Kt = 3.2: **(a-c, g-i)** distribution maps and **(d-f, j-l)** profiles at the notch root of **(a, d, g, j)** maximum principal stress, **(b, e, h, k)** equivalent plastic strain, and **(c, f, i, l)** local hydrogen content. The positions of the initial cracks determined from **Figure 7** are also indicated in each profile. For both the specimens with Kt = 2.1 and Kt = 3.2, the peaks of the maximum principal stress and local hydrogen contents were several

hundred micrometers away from the notch root surfaces, while the plastic strains were maximum at the surfaces of notch root. Accordingly, it can be said that the initiation sites of the quasi-cleavage cracks correspond with the positions where the plastic strains are maximum.

The results shown in **Figures 7 and 8** strongly suggest that plastic deformation is important for quasi-cleavage cracking. Then, we analyzed the local plastic deformation behavior around the notch root for the specimen with Kt = 2.1 by using the DIC technique. **Figure 9** shows the DIC analysis result on the free surface of the hydrogen-charged specimen (H_D = 0.41 mass ppm (22.5 at ppm)) after applying the stress until reaching the maximum value approximately: **(a)** an EBSD orientation map, **(b, c)** equivalent plastic strain distribution maps (**(c)** is an enlarged map corresponding to the red rectangle in **(b)**), and **(d)** a {011} pole figure obtained using the orientation of the deformation band with large plastic strain indicated by the red arrow in **(c)**. The distribution of plastic strain is not uniform, and several deformation bands mainly elongating parallel to the block boundaries (black lines) are observed. Crystallographic orientation analysis revealed that the deformation band indicated by the red arrow in **Figure 9(c)** was parallel to the {011} plane trace on the observed section, which corresponded to the habit plane / block boundary of the lath martensite structure. Assuming that the slip system is <111> {011}, the Schmidt factors of simple uniaxial tensile deformation for each {011} plane are listed in **Figure 9(d)**. The listed values are the higher values of the two <111> slip directions on each {011} slip plane. It should be noted that the Schmidt factor of the {011} plane corresponding to the deformation band, i.e., parallel to the

habit plane / block boundary, is not the maximum among the possible six {011} planes. We confirmed that all of the deformation bands developed nearly parallel to the habit plane / block boundary. Accordingly, we can propose that the concentration of plastic strain along habit planes / block boundaries results in quasi-cleavage cracking. The formation of deformation bands parallel to the habit plane is not a unique characteristic of the hydrogen-charged specimen. We confirmed the same tendency in the uncharged specimen. Previous studies [36-38] reported that the slip systems, whose slip planes were parallel to habit planes / block boundaries, were preferentially operated in lath martensite structures.

The plastic strain values around the notch roots were evaluated in order to confirm the hydrogen-enhanced localized plasticity (HELP) effect [1, 39-41]. As the plastic strain distribution determined by DIC was not uniform, as shown in **Figure 9**, we measured the average plastic strain values along the five parallel lines whose intervals along the tensile direction were 50 μm. **Figure 10** shows (a) the profiles of plastic strain values as a function of the distance from the notch root surface (blue: the uncharged specimen, red: the hydrogen-charged specimen, and black: the FE simulation result on the specimen surface), (b, c) DIC analysis results where the positions of the plastic strain value measurements are indicated (b: uncharged specimen, c: hydrogen-charged specimen). The plastic strain values determined by DIC in the uncharged and the hydrogen-charged specimens are nearly equal to the FE simulation results. We find that the hydrogen-charged specimen exhibits larger plastic strain values compared to the uncharged

specimen, although the difference is small. This suggests that hydrogen enhanced the dislocation mobility and increased the plastic strain value under the same stress level. As a result, the DIC analysis confirmed that hydrogen promoted the local plastic deformation, i.e., HELP effect occurred.

4. Discussion

When the H_D was large (2.21 mass ppm (121 at ppm)), the initial cracks were of the intergranular-type at the prior austenite grain boundaries for both the specimens with Kt = 2.1 and Kt = 3.2, as shown in **Figure 5**. We found that the crack initiation sites corresponded to the areas where both the maximum principal stress and the local hydrogen content were high. Moreover, the maximum principal stress and the local hydrogen content at the crack initiation sites for the specimens with Kt = 2.1 and Kt = 3.2 exhibited similar values (σ_P = 1257 ~ 1283 MPa and H_L = 143 ~ 144 at ppm for Kt = 2.1, σ_P = 1212 MPa, and H_L = 159 at ppm for Kt = 3.2). This suggests that the intergranular cracks were initiated under almost the same local stress field and hydrogen content, even though the stress concentration factors of the specimens were different. Wang et al. [9] also proposed that the local stress and hydrogen content were the key factors for hydrogen-related intergranular cracking. Previously, we studied the local hydrogen accumulation behavior of martensitic steels during deformation by utilizing hydrogen micro-printing technique [20, 32]. The results suggested that hydrogen tended to accumulate around the prior austenite grain

boundaries during deformation, and the high hydrogen content at the prior austenite grain boundary led to intergranular cracking. The present FE simulations used a continuum body and did not consider the accumulation of hydrogen around the prior austenite grain boundaries. We can assume that hydrogen accumulated more locally around the prior austenite grain boundaries, which existed at the position with high hydrogen content in the FE simulations (**Figures 6 (c, i)**). It is reasonable to consider that the high principal stress and the high hydrogen content can induce hydrogen-related decohesion. Accordingly, we can conclude that the intergranular cracking originated from stress-controlled decohesion at the prior austenite grain boundary.

When the H_D was small (0.41 mass ppm (22.5 at ppm)), the quasi-cleavage cracks formed at the surface of the notch root and propagated along the {011} planes (**Figure 7**). As shown in **Figure 8**, the maximum principal stress and the local hydrogen content does not exhibit the maximum value at the initiation sites of the quasi-cleavage cracks, i.e., the notch root surface, although these values are relatively high at the notch root surface. It is a common understanding that hydrogen-related decohesion is most likely to occur at the position with the highest principal stress and hydrogen content. The results shown in **Figures 7 and 8** strongly suggest that the quasi-cleavage cracking was not due to simple decohesion of particular atomic planes and / or boundaries, though several previous papers proposed that quasi-cleavage cracking originated from hydrogen-enhanced decohesion [22-25]. ~~The crystallographic feature of the quasi-cleavage cracks, i.e., {011} crack plane, supports this notion because typical cleavage plane of a bcc crystal is {001} plane.~~ **Figures**

7 and 8 demonstrate that the initiation sites of quasi-cleavage cracking correspond to the positions with the largest plastic strain. Based on these results, we can conclude that the quasi-cleavage cracking was closely related to the local plastic deformation on the {011} planes. Birnbaum et al. first proposed the HELP effect [39], and several studies directly observed the HELP effect using in situ high-voltage transmission electron microscopy deformation experiments [40, 41]. The DIC analysis, shown in **Figure 10**, confirms that hydrogen enhanced the local plastic deformation, although the analysis was performed on the free surface of the specimen and the increase in plastic strain value due to the existence of hydrogen was not significant. The first-principles calculations by Matsumoto et al. [42] suggested that hydrogen reduced the vacancy formation energy and increased the activation energy for vacancy diffusion. Accordingly, one possible explanation for the mechanism of hydrogen-related quasi-cleavage cracking is that hydrogen-enhanced local plastic deformation and hydrogen-induced stabilization of vacancy promote coalescence of micro-voids on the {011} operated slip planes. Morsdof et al. reported that plastic deformation was localized around block boundaries [38]. Considering the deformation localization would increase local stress field and local hydrogen concentration around the block boundaries, hydrogen might induce decohesion at block boundaries. Actually, as described above, several papers insisted that the hydrogen-related quasi-cleavage fracture occurred on lath boundaries and / or block boundaries in martensite structure [22-25]. However, we previously showed the clear evidence that the quasi-cleavage crack propagated inside the lath, not on the lath boundaries [12]. As shown in

Figures 7 and 8, the present study revealed that the initiation sites of quasi-cleavage cracking correspond to the positions with the largest plastic strain, not likely condition for simple decohesion. Moreover, one can easily confirm that there are several crack components which are not parallel to but across the block boundaries in **Figure 7 (b, d)** (though these are two-dimensional observations). Based on these facts, decohesion of lath and / or block boundaries would not be a common feature of hydrogen-related quasi-cleavage fracture. Compared with the case of the intergranular cracking, the local condition for the initiation of the quasi-cleavage cracking was not simple. The FE simulation results in **Figure 8** show that the local values of the maximum principal stress, plastic strain ~~amount~~, and hydrogen content at the quasi-cleavage crack initiation sites differ depending on the stress concentration factor. Further studies are necessary to understand the local critical condition for the initiation of quasi-cleavage cracking.

5. Conclusions

In the present study, we investigated the hydrogen-related fracture behavior of specimens with different stress concentration factors through microstructure observation, FE simulation, and DIC analysis. The following conclusions are drawn.

(1) When the H_D was large (2.21 mass ppm (121 at ppm)), both the specimens with Kt = 2.1 and Kt = 3.2 were fractured within the apparent elastic strain regime. The EBSD orientation analysis revealed that the crack formed and propagated around the prior austenite grain boundaries.

Through the FE simulations, we found that the crack initiation sites corresponded to the region with high stress and high hydrogen content. Even though the specimen geometries (stress concentration factors) were different, local states, i.e., stress level and hydrogen content, at the crack initiations were almost the same. This indicates that the hydrogen-related intergranular fracture originated from stress-controlled decohesion at the prior austenite grain boundaries.

(2) The specimen with small H_D (0.41 mass ppm (22.5 at ppm)) were fractured after exhibiting some plastic deformation. The quasi-cleavage cracks formed at the surface of the notch root and propagated along the {011} plane traces. The FE simulations revealed that the plastic strains were maximum at the quasi-cleavage crack initiation sites. Moreover, we confirmed that hydrogen enhanced local plastic deformation. Accordingly, we concluded that the quasi-cleavage cracking was closely related to the local plastic deformation on the {011} slip planes. As the local values of maximum principal stress, plastic strain ~~amount~~, and hydrogen content at the initiation sites of the quasi-cleavage cracks were different depending on the stress concentration factor, the critical quantitative condition for the initiation of quasi-cleavage cracking was not simple compared to that of the case of intergranular cracking.

Acknowledgements

This study was financially supported by JSPS KAKENHI Grant Number JP15H04158, JP15H05767, JP19H02459, JP20K21083, the Elements Strategy Initiative for Structural Materials

(ESISM) from MEXT Japan. In addition, this study is based on results obtained from a project commissioned by the New Energy and Industrial Technology Development Organization (NEDO).

References

[1] I.M. Robertson, P. Sofronis, A. Nagao, M.L. Martin, S. Wang, D.W. Gross, K.E. Nygren, Hydrogen embrittlement understood, Metallurgical and Materials Transactions B 46 (2015) 1085-1103.

[2] M. Dadfarnia, A. Nagao, S. Wang, M.L. Martin, B.P. Somerday, P. Sofronis, Recent advances on hydrogen embrittlement of structural materials, International Journal of Fracture 196 (2015) 223-243.

[3] S. Morito, X. Huang, T. Furuhara, T. Maki, N. Hansen, The morphology and crystallography of lath martensite in alloy steels, Acta Materialia, 54 (2006) 5323-5331.

[4] M. Yamaguchi, J. Kameda, K.-I. Ebihara, M. Itakura, H. Kaburaki, Mobile effect of hydrogen on intergranular decohesion of iron: first-principles calculations, Philosophical Magazine 92 (2012) 1349-1368.

[5] K.N. Solanki, M.A. Tschopp, M.A. Bhatia, N.R. Rhodes, Atomistic investigation of the role of grain boundary structure on hydrogen segregation and embrittlement in α-Fe, Metallurgical and Materials Transactions A 44 (2013) 1365-1375.

[6] M. Yamaguchi, K. Ebihara, M. Itakura, Multiscale thermodynamic analysis on hydrogen-induced intergranular cracking in an alloy steel with segregated solutes, Corros Rev 33

(2015) 547-557.

[7] S.K. Banerji, C.J. McMahon Jr, H.C. Feng, Intergranular fracture in 4340-type steels: effects of impurities and hydrogen, Metallurgical and Materials Transactions A 9A (1978) 237-247.

[8] B. Craig, G. Krauss, The structure of tempered martensite and its susceptibility to hydrogen stress cracking, Metallurgical and Materials Transactions A 11A (1980) 1799-1808.

[9] M. Wang, E. Akiyama, K. Tsuzaki, Effect of hydrogen and stress concentration on the notch tensile strength of AISI 4135 steel, Materials Science and Engineering A 398 (2005) 37-46.

[10] A. Shibata, T. Murata, H. Takahashi, T. Matsuoka, N. Tsuji, Characterization of hydrogen-related fracture behavior in as-quenched low-carbon martensitic steel and tempered medium-carbon martensitic steel, Metallurgical and Materials Transactions A 46 (2015) 5685-5696.

[11] A. Shibata, T. Matsuoka, A. Ueno, N. Tsuji, Fracture surface topography analysis of the hydrogen-related fracture propagation process in martensitic steel, International Journal of Fracture 205 (2017) 73-82.

[12] A. Shibata, Y. Momotani, T. Murata, T. Matsuoka, M. Tsuboi, N. Tsuji, Microstructural and crystallographic features of hydrogen-related fracture in lath martensitic steels, Materials Science and Technology 33 (2017) 1524-1532.

[13] A. Shibata, Y. Madi, K. Okada, N. Tsuji, J. Besson, Mechanical and microstructural analysis on hydrogen-related fracture in a martensitic steel, International Journal of Hydrogen Energy 44 (2019) 29034-29046.

[14] S.P. Lynch, A Fractographic Study on Gaseous Hydrogen embrittlement and liquid-metal embrittlement in a tempered-martensitic steel, Acta Metallurgica 32 (1984) 79-90.

[15] M.L. Martin, J.A. Fenske, G.S. Liu, P. Sofronis, I.M. Robertson, On the formation and nature of quasi-cleavage fracture surfaces in hydrogen embrittled steels, Acta Materialia 59 (2011) 1601-1606.

[16] Y. Hagihara, T. Shobu, N. Hisamori, H. Suzuki, K. Takai, K. Hirai, Delayed fracture using CSRT and hydrogen trapping characteristics of V-bearing high-strength steel, ISIJ International 52 (2012) 298-306.

[17] Y. Takeda, C.J. McMahon Jr, Strain controlled vs stress controlled hydrogen induced fracture in a quenched and tempered steel, Metallurgical and Materials Transactions A 12A (1981) 1255-1266.

[18] P. Novak, R. Yuan, B.P. Somerday, P. Sofronis, R.O. Ritchie, A statistical, physical-based, micro-mechanical model of hydrogen-induced intergranular fracture in steel, Journal of the Mechanics and Physics of Solids 58 (2010) 206-226.

[19] A. Shibata, H. Takahashi, N. Tsuji, Microstructural and crystallographic features of hydrogen-related crack propagation in low carbon martensitic steel, ISIJ International 52 (2012) 208-212.

[20] Y. Momotani, A. Shibata, D. Terada, N. Tsuji, Effect of strain rate on hydrogen embrittlement in low-carbon martensitic steel, International Journal of Hydrogen Energy 42 (2017) 3371-3379.

[21] K. Okada, A. Shibata, Y. Takeda, N. Tsuji, Crystallographic feature of hydrogen-related fracture in 2Mn-0.1C ferritic steel, International Journal of Hydrogen Energy 43 (2018) 11298-11306.

[22] Y.H. Kim, J.W. Morris Jr, The nature of quasicleavage fracture in tempered 5.5Ni steel after hydrogen charging, Metallurgical Transactions A 14A (1983) 1883-1888.

[23] Y.H. Kim, H.J. Kim, J.W. Morris Jr, The influence of precipitated austenite on hydrogen embrittlement in 5.5Ni steel, Metallurgical and Materials Transactions A 17A (1986) 1157-1164.

[24] A. Nagao, C.D. Smith, M. Dadfarnia, P. Sofronis, I.M. Robertson, The role of hydrogen in hydrogen embrittlement fracture of lath martensitic steel, Acta Materialia 60 (2012) 5182-5189.

[25] G.L. Pioszak, R.P. Gangloff, Hydrogen environment assisted cracking of modern ultra-high strength martensitic steels, Metallurgical and Materials Transactions 48A (2017) 4025-4045.

[26] J. Besson, R. Foerch, Large scale object-oriented finite element code design, Computer Methods in Applied Mechanics and Engineering, 142 (1997) 165-187.

[27] Zset, <http://www.zset-software.com>. 2015).

[28] P. Sofronis, R.M. McMeeking, Numerical analysis of hydrogen transport near a blunting crack tip, Journal of the Mechanics and Physics of Solids 37 (1989) 317-350.

[29] D.C. Ahn, P. Sofronis, R. Dodds, Modeling of hydrogen-assisted ductile crack propagation in metals and alloys, International Journal of Fracture 145 (2007) 135-157.

[30] R.A. Oriani, The diffusion and trapping of hydrogen in steel, Acta Metallurgica 18 (1970)

147-157.

[31] A. Seeger, On the location of positive muons and solute hydrogen atoms in alpha iron, Physics Letters, 58A (1976) 137-138.

[32] Y. Momotani, A. Shibata, T. Yonemura, Y. Bai, N. Tsuji, Effect of initial dislocation density on hydrogen accumulation behavior in martensitic steel, Scripta Materialia 178 (2020) 318-323.

[33] W.Y. Choo, J.Y. Lee, Thermal analysis of trapped hydrogen in pure iron, Metallurgical transactions A 13 A (1982) 135-140.

[34] A. Taha, P. Sofronis, A micromechanics approach to the study of hydrogen transport and embrittlement, Engineering Fracture Mechanics 68 (2001) 803-837.

[35] S. Harjo, T. Kawasaki, Y. Tomota, W. Gong, K. Aizawa, G. Tichy, Z. Shi, T. Ungár, Work hardening, dislocation structure, and load partitioning in lath martensite determined by in situ neutron diffraction line profile analysis, Metallurgical and Materials Transactions A 48 (2017) 4080-4092.

[36] S. Nambu, M. Michiuchi, Y. Ishimoto, K. Asakura, J. Inoue, T. Koseki, Transition in deformation behavior of martensitic steel during large deformation under uniaxial tensile loading, Scripta Materialia 60 (2009) 221-224.

[37] M. Michiuchi, S. Nambu, Y. Ishimoto, J. Inoue, T. Koseki, Relationship between local deformation behavior and crystallographic features of as-quenched lath martensite during uniaxial tensile deformation, Acta Materialia 57 (2009) 5283-5291.

[38] L. Morsdorf, O. Jeannin, D. Barbier, M. Mitsuhara, D. Raabe, C.C. Tasan, Multiple mechanisms of lath martensite plasticity, Acta Materialia, 12 (2016) 202-214.

[39] H.K. Birnbaum, P. Sofronis, Hydrogen-enhanced localized plasticity--a mechanism for hydrogen-related fracture, Materials Science and Engineering A176 (1994) 191-202.

[40] P.J. Ferreira, I.M. Robertson, H.K. Birnbaum, Hydrogen effects on the interaction between dislocations, Acta Materialia 46 (1998) 1749-1757.

[41] I.M. Robertson, The effect of hydrogen on dislocation dynamics, Engineering Fracture Mechanics 64 (1999) 649-673.

[42] R. Matsumoto, N. Nishiguchi, S. Taketomi, N. Miyazaki, First-principles calculation of hydrogen effects on the formation and diffusion of vacancies in alpha Iron: discussion of the hydrogen-enhanced strain-Induced vacancy mechanism, Zairyo/Journal of the Society of Materials Science, Japan 63 (2014) 182-187.

Figure captions

Figure 1 Schematic illustrations of (a) the double-notched tensile test specimen (unit: mm) and (b) the FE meshes (one-eighth of the specimen geometry).

Figure 2 Desorption profiles of the hydrogen-charged specimens at the current densities of 0.625 A m^{-2} (open circles) and 1 A m^{-2} (solid circles).

Figure 3 Engineering stress – displacement curves of the specimens with (a) Kt = 2.1 and (b) Kt = 3.2.

Figure 4 SEM images showing the fracture surfaces of the hydrogen-charged specimen with Kt = 2.1 and H_D = 2.21 mass ppm (121 at ppm): (a) low magnification image and (b-d) high magnification images. The positions of relatively smooth intergranular surface and intergranular-like surface with serrated markings are indicated by the white arrows and the black arrows, respectively, in (d).

Figure 5 (a, c) SEM images and (b, d) EBSD orientation maps around the notch roots of the hydrogen-charged specimens with H_D = 2.21 mass ppm (121 at ppm): (a, b) the specimen with Kt = 2.1 and (c, d) the specimen with Kt = 3.2.

Figure 6 FE simulation results on the mid-thickness sections when H_D is 2.21 mass ppm (121 at ppm) for the specimen with (a-f) Kt = 2.1 and (g-l) Kt = 3.2: (a-c, g-i) distribution maps and (d-f, j-l) profiles at the notch root of (a, d, g, j) maximum principal stress, (b, e, h, k) equivalent plastic strain, and (c, f, i, l) local hydrogen content.

Figure 7 (a, c) SEM images and (b, d) EBSD orientation maps around the notch roots of the hydrogen-charged specimens with H_D = 0.41 mass ppm (22.5 at ppm): (a, b) the specimen with Kt = 2.1 and (c, d) the specimen with Kt = 3.2.

Figure 8 FE simulation results on the mid-thickness sections when H_D is 0.41 mass ppm (22.5 at ppm) for the specimen with (a-f) Kt = 2.1 and (g-l) Kt = 3.2: (a-c, g-i) distribution maps and (d-f, j-l) profiles at the notch root of (a, d, g, j) maximum principal stress, (b, e, h, k) equivalent plastic strain, and (c, f, i, l) local hydrogen content.

Figure 9 DIC analysis result of the hydrogen-charged specimen (Kt = 2.1, H_D = 0.41 mass ppm (22.5 at ppm)) after applying stress until reaching around the maximum value: (a) an EBSD orientation map, (b, c) equivalent plastic strain distribution maps ((c) is an enlarged one corresponding to the red rectangle in (b)), and (d) a {011} pole figure obtained using the orientation of the deformation band with large plastic strain indicated by the red arrow in (c).

Figure 10 (a) Profiles of plastic strain value as a function of the distance from the notch root surface (Kt = 2.1). Blue: the uncharged specimen, red: the hydrogen-charged specimen (H_D = 0.41 mass ppm (22.5 at ppm)), and black: the FE simulation result. (b, c) DIC analysis results where the positions of the plastic strain value measurements are indicated (b: uncharged specimen, c: hydrogen-charged specimen).

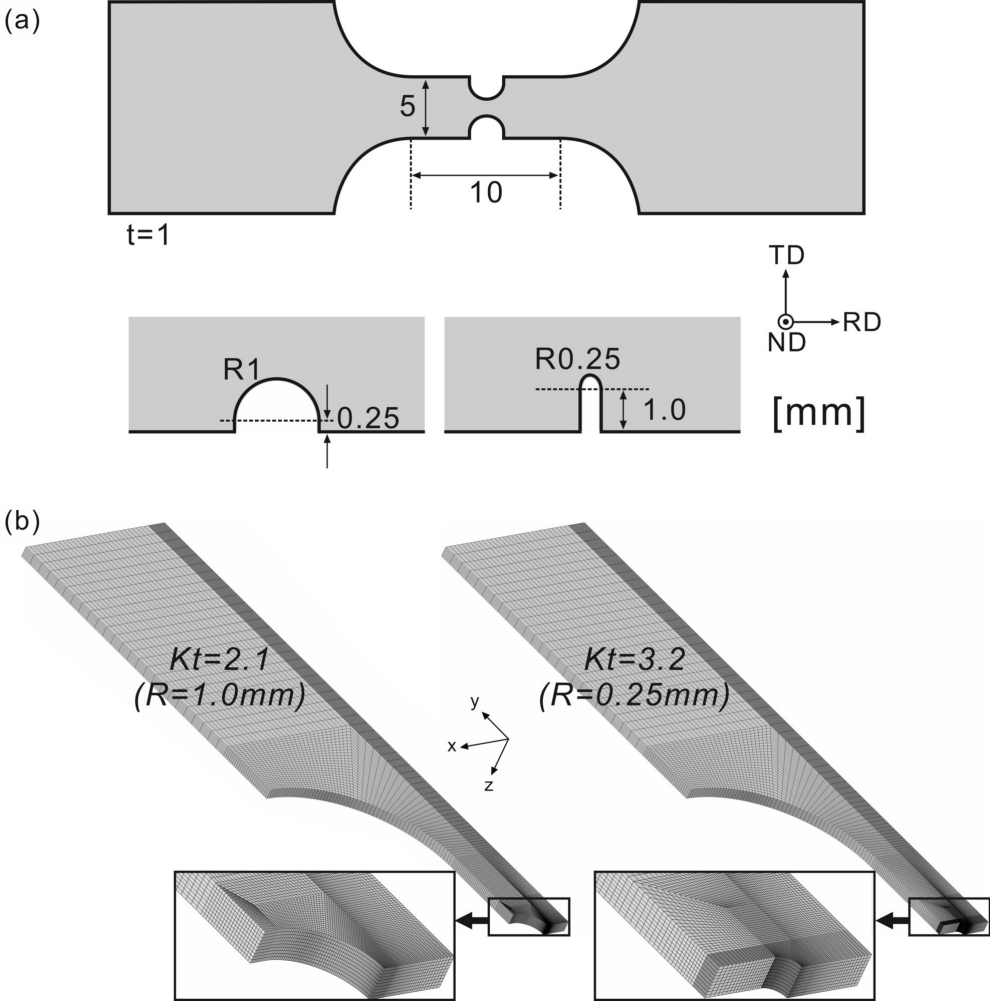
(a)
5
10
t=1
TD
RD
ND
R1
0.25
R0.25
1.0
[mm]
(b)
Kt=2.1
(R=1.0mm)
Kt=3.2
(R=0.25mm)
y
x
z

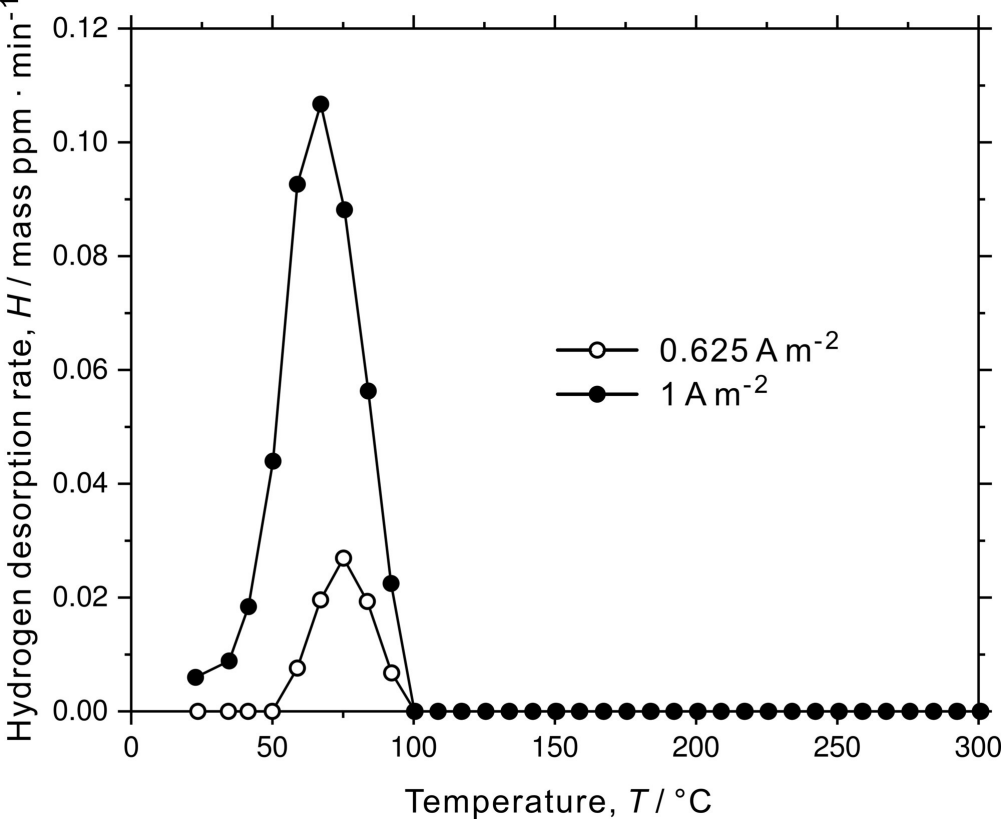
Hydrogen desorption rate, H / mass ppm · min-1
0.12
0.10
0.08
0.06
0.04
0.02
0.00
0
50
100
150
200
250
300
Temperature, T / °C
0.625 A m-2
1 A m-2

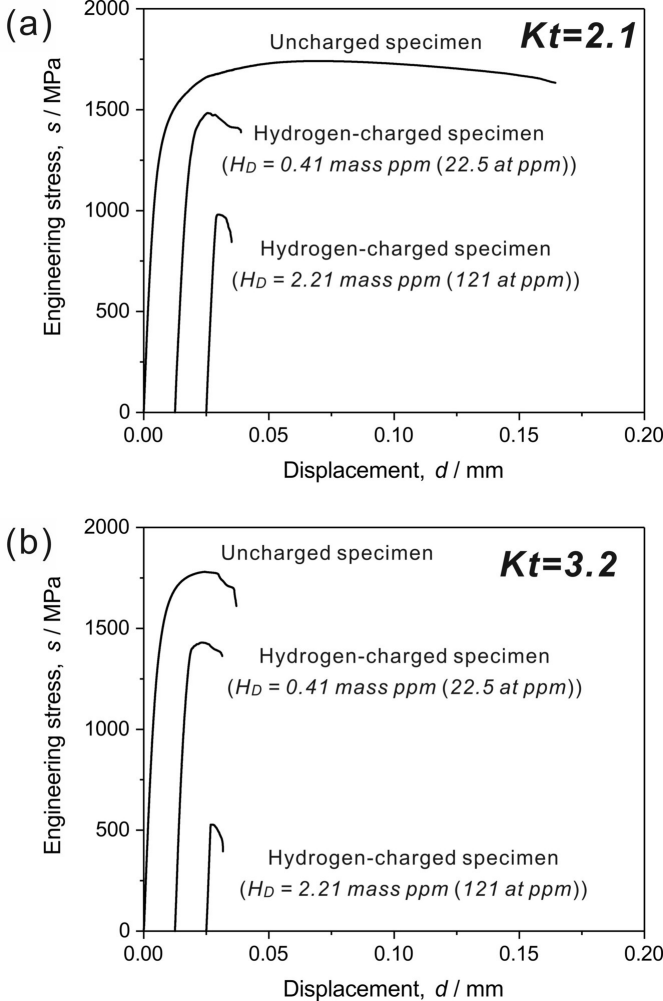
(a)
Kt=2.1
Uncharged specimen
Hydrogen-charged specimen
(H_D = 0.41 mass ppm (22.5 at ppm))
Hydrogen-charged specimen
(H_D = 2.21 mass ppm (121 at ppm))
Engineering stress, s / MPa
Displacement, d / mm
2000
1500
1000
500
0
0.00
0.05
0.10
0.15
0.20
(b)
Kt=3.2
Uncharged specimen
Hydrogen-charged specimen
(H_D = 0.41 mass ppm (22.5 at ppm))
Hydrogen-charged specimen
(H_D = 2.21 mass ppm (121 at ppm))
Engineering stress, s / MPa
Displacement, d / mm

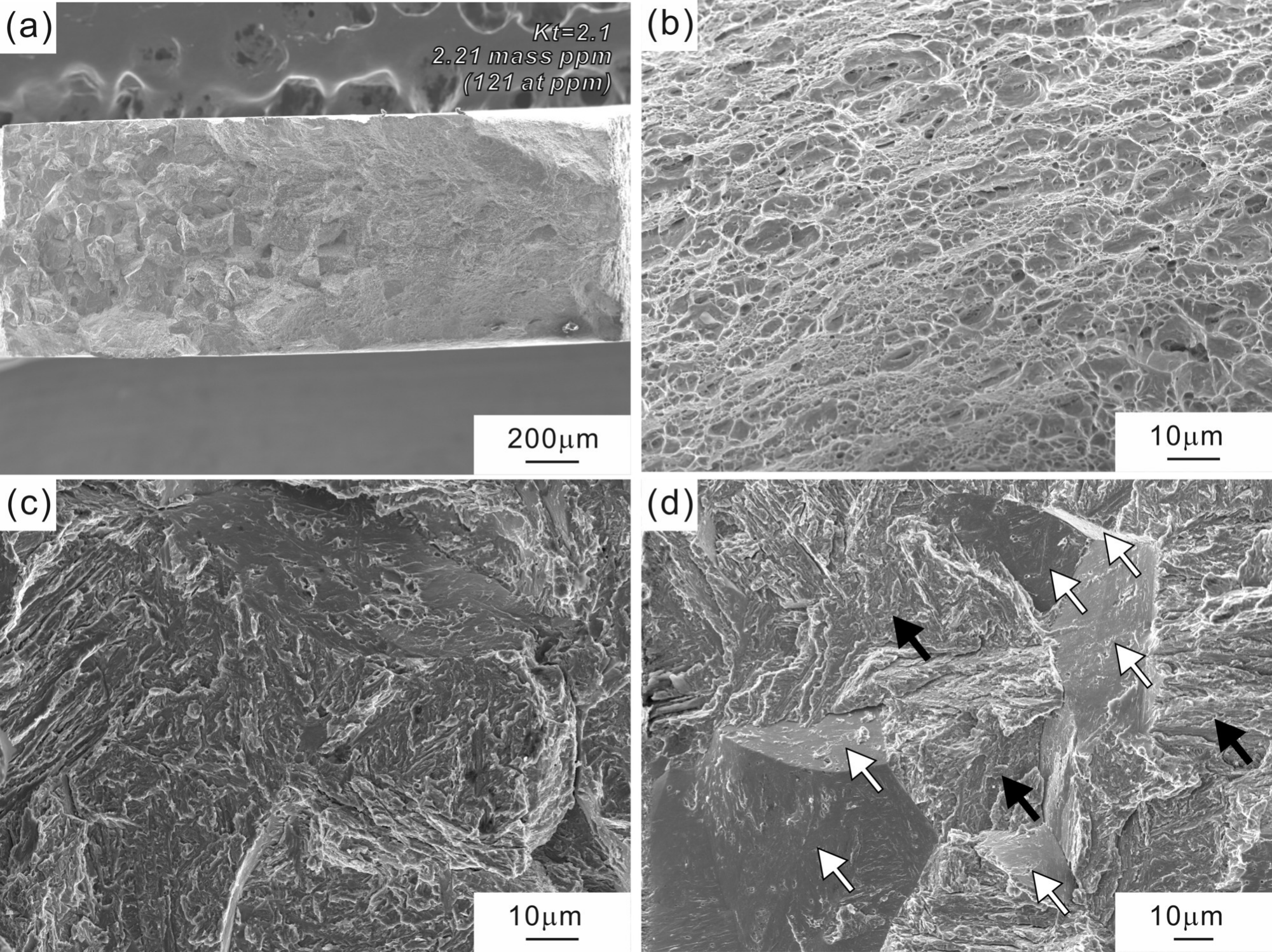
(a)
Kt=2.1
2.21 mass ppm
(121 at ppm)
200μm
(b)
10μm
(c)
10μm
(d)
10μm

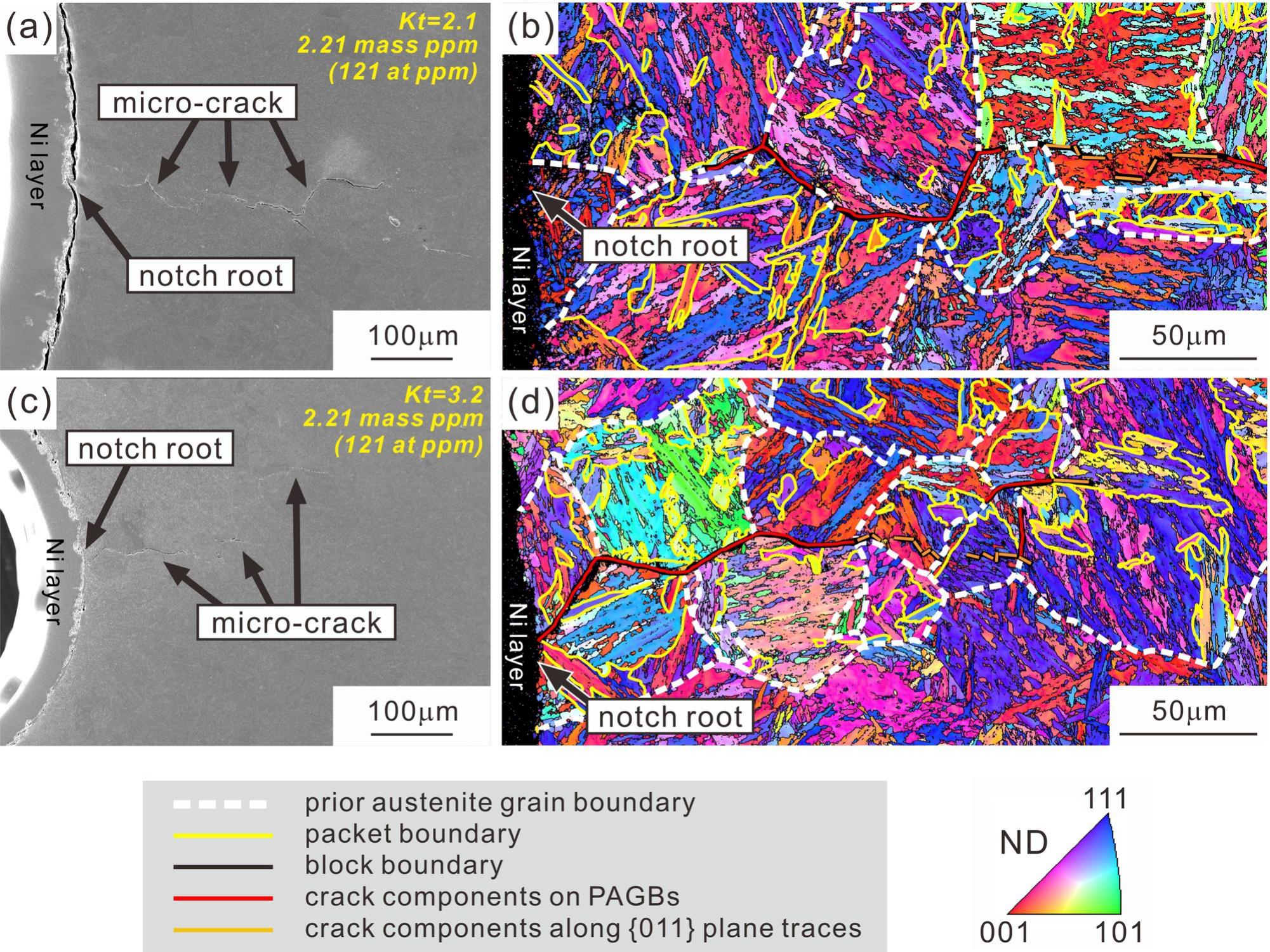
(a)
Kt=2.1
2.21 mass ppm
(121 at ppm)
micro-crack
Ni layer
notch root
100μm
(b)
notch root
Ni layer
50μm
(c)
Kt=3.2
2.21 mass ppm
(121 at ppm)
notch root
Ni layer
micro-crack
100μm
(d)
Ni layer
notch root
50μm
prior austenite grain boundary
packet boundary
block boundary
crack components on PAGBs
crack components along {011} plane traces
111
ND
001
101

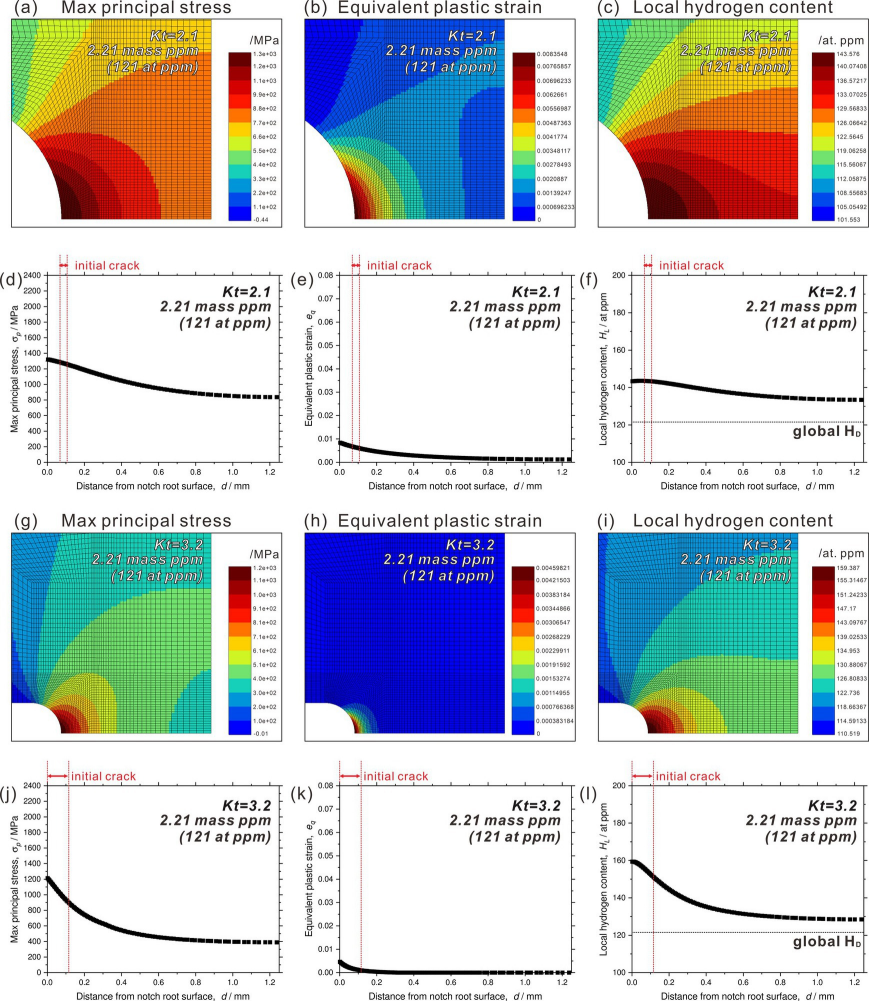
(a) Max principal stress
Kt=2.1
2.21 mass ppm
(121 at ppm)
/MPa
1.3e+03
1.2e+03
1.1e+03
9.9e+02
8.8e+02
7.7e+02
6.6e+02
5.5e+02
4.4e+02
3.3e+02
2.2e+02
1.1e+02
-0.44
(b) Equivalent plastic strain
Kt=2.1
2.21 mass ppm
(121 at ppm)
0.0083548
0.0076857
0.0069233
0.0062661
0.0056987
0.0048736
0.0041774
0.0034811
0.0027849
0.0020887
0.0013925
0.0006962
0
(c) Local hydrogen content
Kt=2.1
2.21 mass ppm
(121 at ppm)
/at. ppm
143.876
140.07408
136.57217
133.07025
129.56833
126.06642
122.5645
119.06258
115.56067
112.05875
108.55683
105.05492
101.553
initial crack
(d)
Kt=2.1
2.21 mass ppm
(121 at ppm)
Max principal stress, σp / MPa
Distance from notch root surface, d / mm
initial crack
(e)
Kt=2.1
2.21 mass ppm
(121 at ppm)
Equivalent plastic strain, εp
Distance from notch root surface, d / mm
initial crack
(f)
Kt=2.1
2.21 mass ppm
(121 at ppm)
Local hydrogen content, HL / at.ppm
global HD
Distance from notch root surface, d / mm
(g) Max principal stress
Kt=3.2
2.21 mass ppm
(121 at ppm)
/MPa
1.2e+03
1.1e+03
1.0e+03
9.1e+02
8.1e+02
7.1e+02
6.1e+02
5.1e+02
4.0e+02
3.0e+02
2.0e+02
1.0e+02
-0.01
(h) Equivalent plastic strain
Kt=3.2
2.21 mass ppm
(121 at ppm)
0.0045821
0.0042153
0.0038318
0.0034486
0.0030654
0.0026822
0.0022991
0.0019159
0.0015327
0.0011495
0.0007663
0.0003831
0
(i) Local hydrogen content
Kt=3.2
2.21 mass ppm
(121 at ppm)
/at. ppm
159.387
155.31467
151.24233
147.17
143.09767
139.02533
134.953
130.88067
126.80833
122.736
118.66367
114.59133
110.519
initial crack
(j)
Kt=3.2
2.21 mass ppm
(121 at ppm)
Max principal stress, σp / MPa
Distance from notch root surface, d / mm
initial crack
(k)
Kt=3.2
2.21 mass ppm
(121 at ppm)
Equivalent plastic strain, εp
Distance from notch root surface, d / mm
initial crack
(l)
Kt=3.2
2.21 mass ppm
(121 at ppm)
Local hydrogen content, HL / at.ppm
global HD
Distance from notch root surface, d / mm

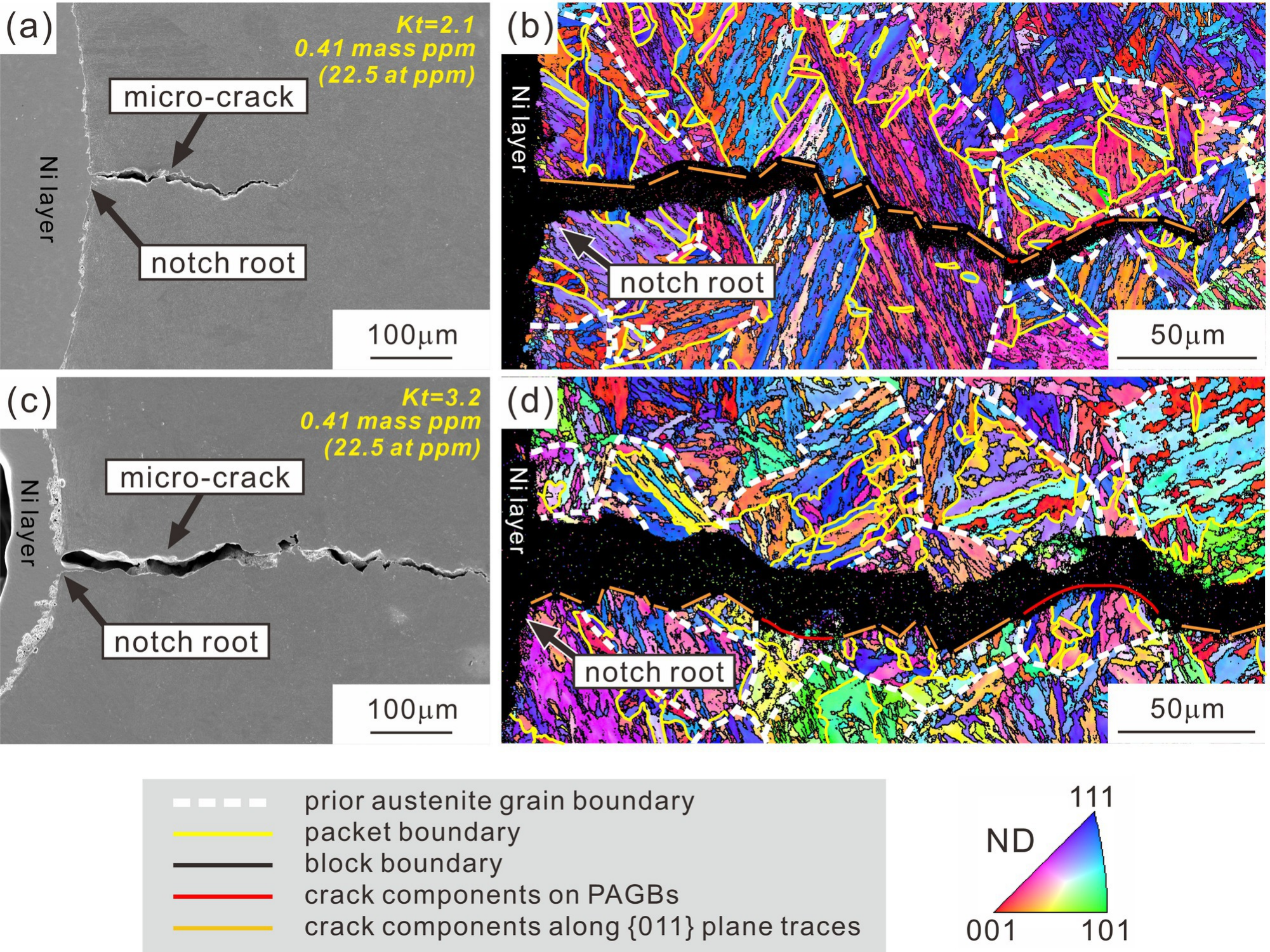
(a)
Kt=2.1
0.41 mass ppm
(22.5 at ppm)
micro-crack
Ni layer
notch root
100μm
(b)
Ni layer
notch root
50μm
(c)
Kt=3.2
0.41 mass ppm
(22.5 at ppm)
micro-crack
Ni layer
notch root
100μm
(d)
Ni layer
notch root
50μm
prior austenite grain boundary
packet boundary
block boundary
crack components on PAGBs
crack components along {011} plane traces
111
ND
001
101

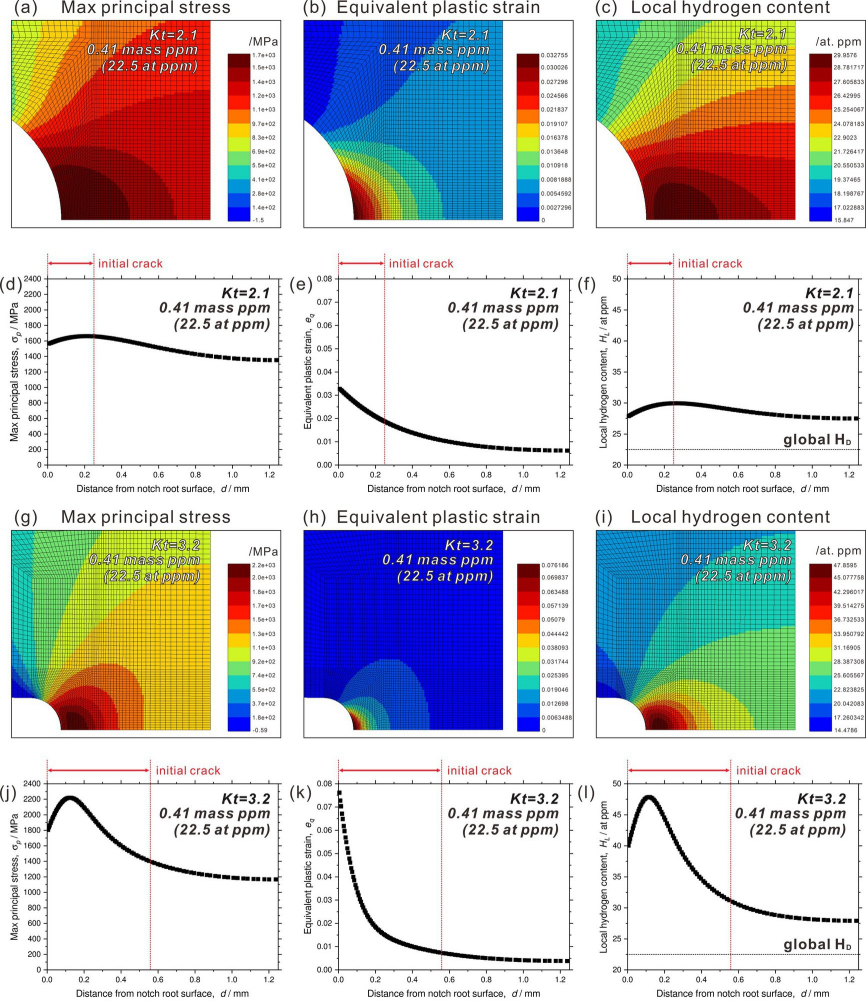
(a) Max principal stress
Kt=2.1
0.41 mass ppm
(22.5 at ppm)
/MPa
1.7e+03
1.5e+03
1.4e+03
1.2e+03
1.1e+03
9.7e+02
8.3e+02
6.9e+02
5.5e+02
4.1e+02
2.8e+02
1.4e+02
-1.5
(b) Equivalent plastic strain
Kt=2.1
0.41 mass ppm
(22.5 at ppm)
0.032755
0.030026
0.027296
0.024566
0.021837
0.019107
0.016378
0.013648
0.010918
0.0081888
0.0054592
0.0027296
0
(c) Local hydrogen content
Kt=2.1
0.41 mass ppm
(22.5 at ppm)
/at. ppm
29.9375
28.781717
27.626433
26.42995
25.254067
24.078183
22.9023
21.726417
20.550533
19.37465
18.198767
17.022883
15.847
initial crack
(d)
Kt=2.1
0.41 mass ppm
(22.5 at ppm)
Max principal stress, σ_p / MPa
Distance from notch root surface, d / mm
initial crack
(e)
Kt=2.1
0.41 mass ppm
(22.5 at ppm)
Equivalent plastic strain, e_p
Distance from notch root surface, d / mm
initial crack
(f)
Kt=2.1
0.41 mass ppm
(22.5 at ppm)
Local hydrogen content, H_L / at ppm
global H_b
Distance from notch root surface, d / mm
(g) Max principal stress
Kt=3.2
0.41 mass ppm
(22.5 at ppm)
/MPa
2.2e+03
2.0e+03
1.8e+03
1.7e+03
1.5e+03
1.3e+03
1.1e+03
9.2e+02
7.4e+02
5.5e+02
3.7e+02
1.8e+02
-0.59
(h) Equivalent plastic strain
Kt=3.2
0.41 mass ppm
(22.5 at ppm)
0.076186
0.069837
0.063488
0.057139
0.05079
0.044442
0.038093
0.031744
0.025395
0.019046
0.012698
0.0063488
0
(i) Local hydrogen content
Kt=3.2
0.41 mass ppm
(22.5 at ppm)
/at. ppm
47.8595
45.077758
42.296017
39.514275
36.732533
33.950792
31.16905
28.387308
25.605567
22.823825
20.042083
17.260342
14.4786
initial crack
(j)
Kt=3.2
0.41 mass ppm
(22.5 at ppm)
Max principal stress, σ_p / MPa
Distance from notch root surface, d / mm
initial crack
(k)
Kt=3.2
0.41 mass ppm
(22.5 at ppm)
Equivalent plastic strain, e_p
Distance from notch root surface, d / mm
initial crack
(l)
Kt=3.2
0.41 mass ppm
(22.5 at ppm)
Local hydrogen content, H_L / at ppm
global H_b
Distance from notch root surface, d / mm

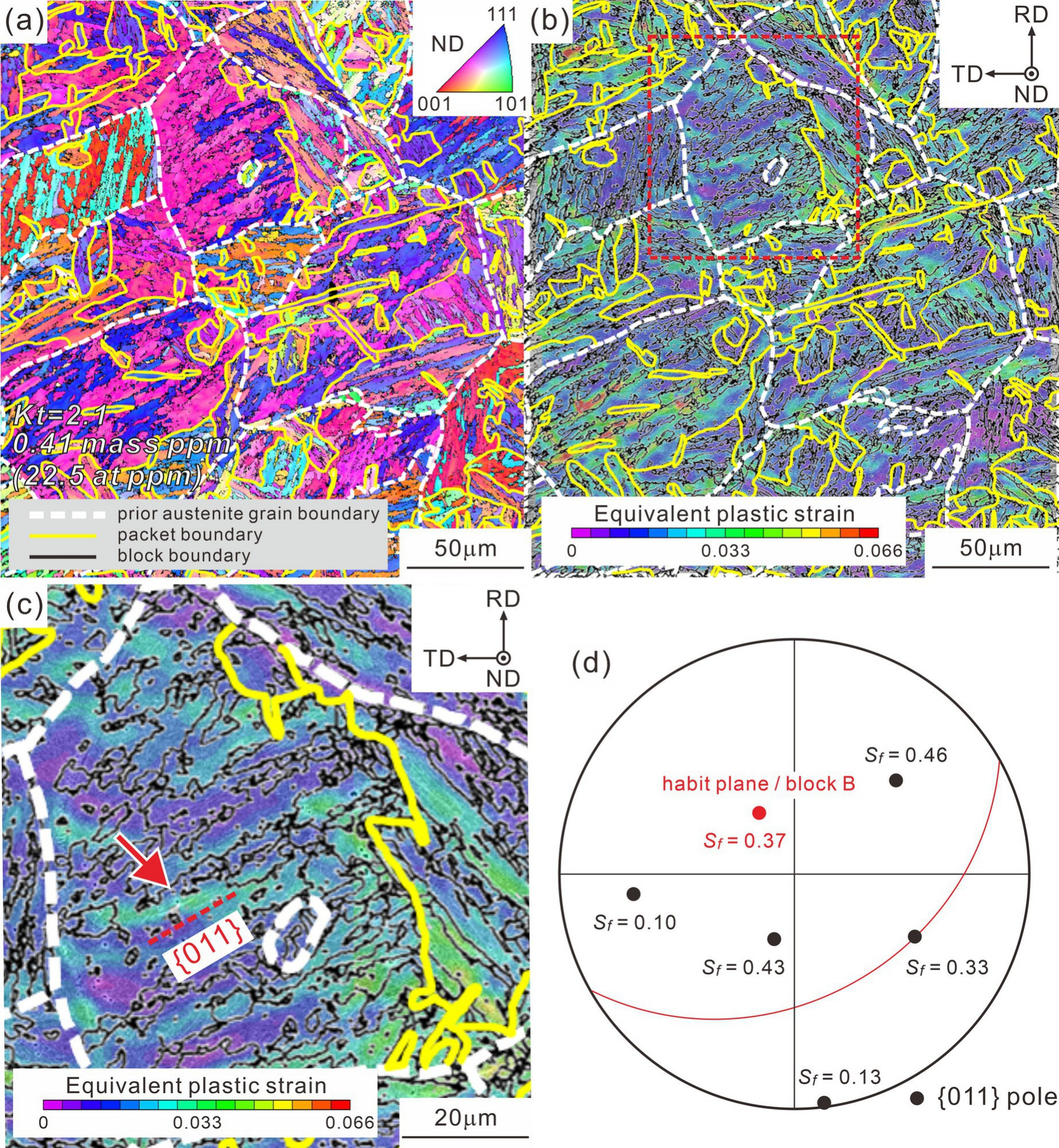
(a)
111
ND
001
101
Kt=2.1
0.41 mass ppm
(22.5 at ppm)
prior austenite grain boundary
packet boundary
block boundary
50μm
(b)
RD
TD
ND
Equivalent plastic strain
0
0.033
0.066
50μm
(c)
RD
TD
ND
{011}
Equivalent plastic strain
0
0.033
0.066
20μm
(d)
S_f = 0.46
habit plane / block B
S_f = 0.37
S_f = 0.10
S_f = 0.43
S_f = 0.33
S_f = 0.13
{011} pole

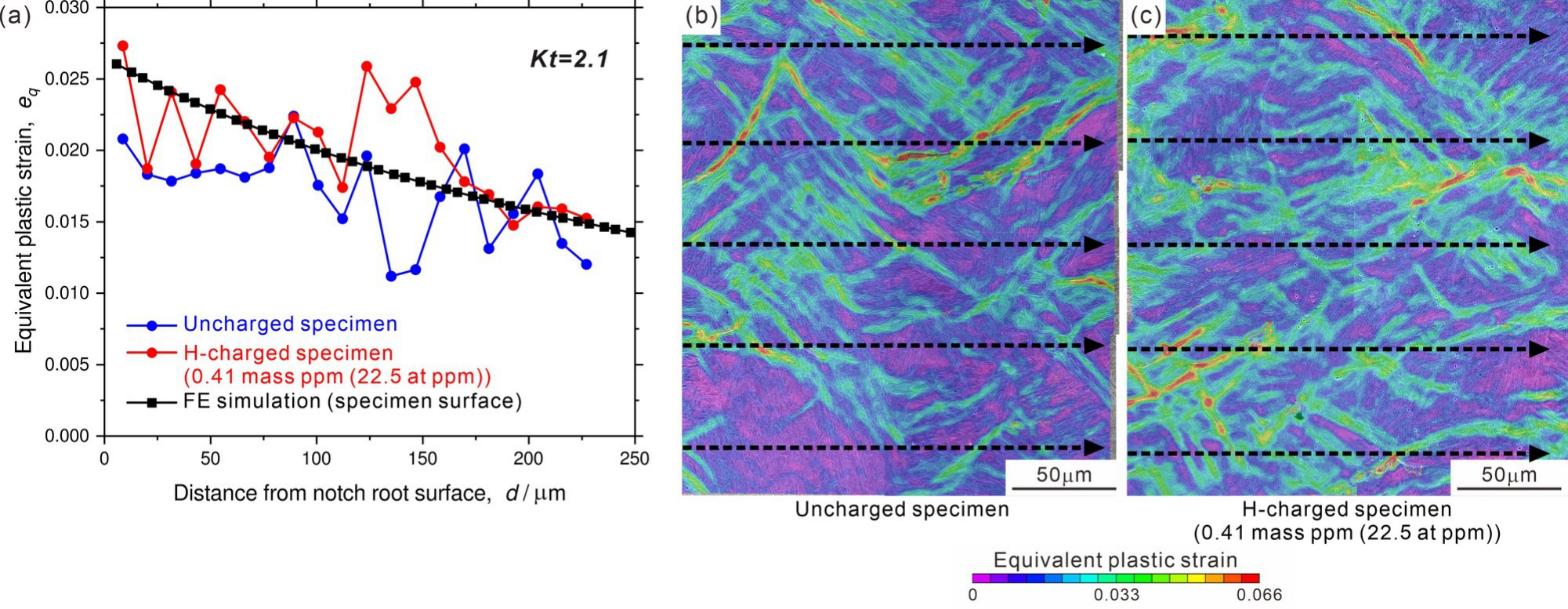
(a)
Kt=2.1
Equivalent plastic strain, e_q
0.030
0.025
0.020
0.015
0.010
0.005
0.000
0
50
100
150
200
250
Distance from notch root surface, d / μm
Uncharged specimen
H-charged specimen
(0.41 mass ppm (22.5 at ppm))
FE simulation (specimen surface)
(b)
(c)
50μm
50μm
Uncharged specimen
H-charged specimen
(0.41 mass ppm (22.5 at ppm))
Equivalent plastic strain
0
0.033
0.066

Intergranular crack initiation

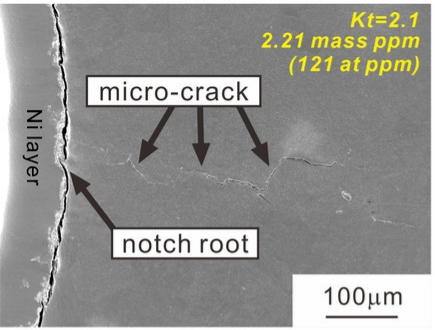

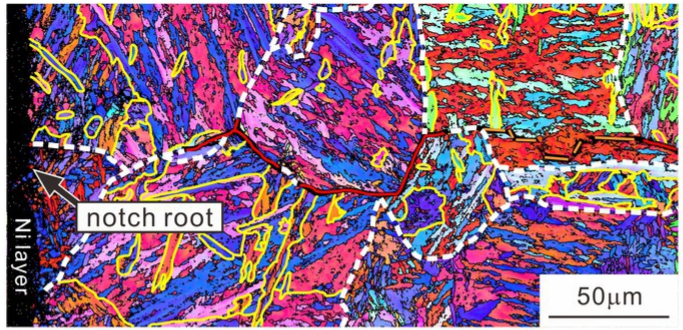

Local hydrogen content

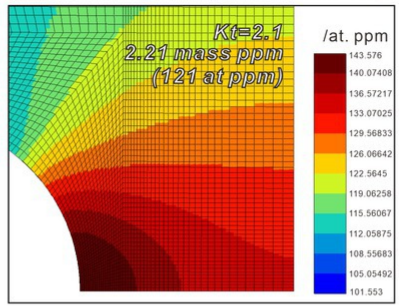

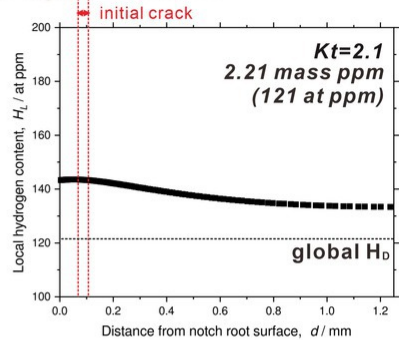

Quasi-cleavage crack initiation

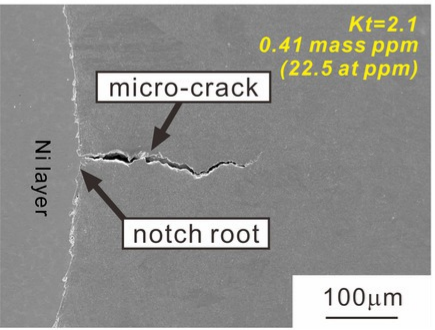

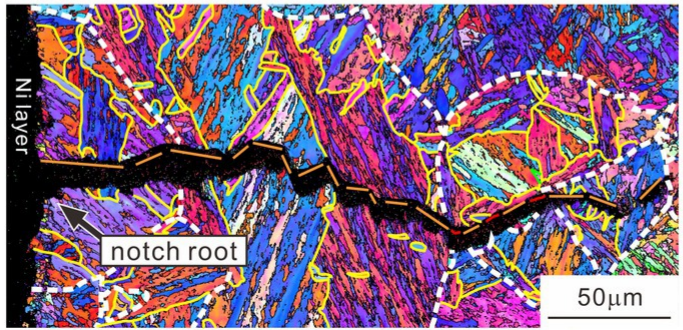

Local hydrogen content